



Experimental investigation of CMT discontinuous wire arc additive manufacturing of Inconel 625

Vojtěch Votruba¹ · Ivan Diviš¹ · Lucie Pilsová² · Pavel Zeman³ · Libor Beránek³ · Jakub Horváth³ · Jan Smolík³

Received: 5 April 2022 / Accepted: 28 July 2022
© The Author(s) 2022

Abstract

Additive manufacturing (AM) is a progressive technology which holds promise for manufacturing of heat resistant super alloys. One of the most productive methods is wire arc additive manufacturing (WAAM). In this article, an alternative WAAM strategy is investigated. Experimental clads and material tests were performed to evaluate the material properties obtained through a cold metal transfer (CMT) discontinuous WAAM of Inconel 625 alloy. Using the modern terminology of Fronius GmbH this method is called CMT cycle step. The difference is that it is automatically controlled by the welding source. CMT discontinuous WAAM has lower productivity and a higher consumption of shielding gas. However, it excels in low heat input and precise material cladding in comparison with a standard CMT continuous WAAM. It enables fabrication of finer details even on thin-walled components or in sections with problematic heat dissipation. Samples manufactured using this strategy were also compared with samples manufactured through a standard CMT continuous WAAM. Two sets of manufactured samples were thus tested. The following material tests were performed: (i) metallographic analysis, (ii) x-ray tomography, (iii) SEM analysis, (iv) hardness, (v) tensile strength (20 °C, 650 °C) and (vi) pin-on-disc (20 °C, 650 °C). The results show that the CMT discontinuous WAAM led to improved material properties in the Inconel 625 samples. Ultimate tensile strength improved by 15% at 20 °C and by 4% at 650 °C. Wear resistance at 650 °C was about two times higher. This paper concludes that the CMT discontinuous WAAM for Inconel 625 is definitely suitable for manufacturing of complex shapes, fine details and thin-walled components.

Keywords Wire arc additive manufacturing · Cold metal transfer · Welding strategy · Inconel 625 · Material properties

1 Introduction

Heat resistant super alloys are considered very important in the aerospace industry, mainly for the application of engine components. Approximately 50% of “hot section”

gas turbine components are manufactured from nickel-based super alloys, as reported in [1, 2]. Nickel-based super alloys are also logical choices in other key industrial sectors such as oil and gas industry components [3] and nuclear power plant components [4]. The main reason for using nickel-based super alloys is their exceptional material characteristics, such as mechanical strength, resistance to surface degradation and creep resistance at elevated temperatures. Many types of nickel-based super alloys have been developed over the years [5]. One commonly used nickel-based super alloy is Inconel 625. Because it contains niobium and molybdenum in a nickel chromium matrix, this super alloy is able to maintain its mechanical properties and corrosion resistance at temperatures up to 650 °C [6]. These excellent properties are retainable even without precipitation heat treatment. Components made from Inconel 625 are widely used in the aerospace industry in the “hot section” of gas

✉ Vojtěch Votruba
V.Votruba@rcmt.cvut.cz

¹ Department of Production Machines and Equipment (RCMT), Faculty of Mechanical Engineering, Czech Technical University, Technická Street 4, 16607 Prague 6, Czech Republic

² Department of Materials Engineering, Faculty of Mechanical Engineering, Czech Technical University, Technická Street 4, 16607 Prague 6, Czech Republic

³ Department of Production Machines and Equipment (RCMT), Faculty of Mechanical Engineering, Center of Advanced Aerospace Technology, Czech Technical University, Technická Street 4, 16607 Prague 6, Czech Republic

Table 1 Composition and properties of Thermanit 625 filler wire material

Chemical composition [wt %]												
C	Si	Mn	P	S	Cr	Mo	Ni	Cu	Ti	Al	Nb	Fe
<0.1	<0.1	<0.1	0.003	0.001	22.3	8.8	64.6	<0.1	0.2	0.2	3.5	0.2
Mechanical properties												
T [°C]	Rp 0.2 [MPa]		Rm [MPa]		A [%]		KV [J]					
20	≥ 460		≥ 740		≥ 30		≥ 60					

turbine engines and in nuclear reactors, the chemical industry and other high temperature and corrosion applications [7–10].

The most common manufacturing method for final products is machining. In general, nickel-based alloys are considered to be difficult-to-cut materials, mainly due to their low thermal conductivity, high hardness and low elastic modulus [1]. This results in a high thermo-mechanical load of the component and the cutting tool. Subsequently, progressive tool wear is observed in machining of nickel-based alloys [11, 12]. In response, new part manufacturing approaches are being explored with the aim of minimizing material removal through the cutting process, which can save both input material and tool costs. Considering current industrial and economical demands, additive manufacturing (AM) of Inconel 625 complex shaped components is one reasonable option [13, 14].

Wire arc additive manufacturing (WAAM) is a subtype of AM that combines wire as a feedstock and electric arc as a heat source [16, 17]. WAAM excels over other metal AM technologies in particular owing to its high deposition rates and low equipment costs [18]. On the other hand, it cannot fully match the geometrical complexity and precision of powder bed AM methods (e.g. selective laser melting or laser metal deposition) [15]. Hence, WAAM is suitable especially for manufacturing or repairing larger components which would typically be machined after an additive process [19–21]. The WAAM of nickel-based super alloys is an important research approach which is not satisfactorily investigated yet.

WAAM techniques can be further categorized by the type of arc welding process. According to current studies [19, 21, 22], three basic techniques are being examined and used for research and development of prototypes. These welding techniques are gas tungsten arc welding (GTAW) [23–25], gas metal arc welding (GMAW) [26–28] and plasma arc welding (PAW) [22, 29]. The advantage of the GMAW process lies in the fact that an electrode is a consumable wire which is standardly coaxial with the welding torch. In contrast, GTAW has the consumable wire added non-coaxially, rendering it more difficult for 5-axis control. While PAW can achieve very high productivity, the heat input is also quite high [30]. It is not beneficial for smaller, more precise parts. Moreover, the PAW process lead and tilt angles of the welding torch could be harmful for the manufacturing result. Thus, the PAW process is not suitable for 5-axis WAAM technology. For the purposes of WAAM, GMAW modification, known as cold metal transfer (CMT), is suitable [31, 32], and it could be an effective approach to solution of manufacturing larger nickel-based super alloy components.

CMT is a modified GMAW process based on short-circuiting transfer, where movement of the wire feedstock at high frequencies (up to 80 Hz) combined with the welding current and voltage control improves the properties of the welding process [34]. The key improvements are elimination of spatter and considerably lower heat input [33]. As an alternative to a standard CMT continuous strategy, a CMT welding unit is also capable of a CMT discontinuous strategy. The process investigated in this paper stops the torch movement and creates a small “puddle weld” [35] by executing a defined

Table 2 Composition and properties of the substrate material S235JRG1 according to EN 10025

Chemical composition [wt %]					
C	Mn	P	S	Cu	N
<0.17	<1.4	<0.035	<0.035	<0.55	<0.012
Mechanical properties					
T [°C]	Rp 0.2 [MPa]	Rm [MPa]	A [%]	KV [J]	
20	≥ 235	≥ 375	≥ 26	≥ 21	

Table 3 Composition of the shielding gas

Chemical composition [wt %]				
CO ₂	H ₂	He	Ar	
0.12	2.0	30.0	67.88	

number of CMT cycles [34] than the torch moves to another “spot”. Shielding gas flow continues through whole process which means the shielding gas consumption is higher as it blows even between welding “spots”. Used CMT discontinuous process creates small “puddle welds” in a frequency circa 1 Hz (do not be confused with frequency of CMT droplets which is up to 80 Hz [34]), and it is approximately two times slower than standard CMT continuous process. This means the CMT discontinuous WAAM strategy has lower productivity and higher consumption of shielding gas. However, it excels in terms of very low heat input and very precise material cladding in comparison with a standard CMT continuous WAAM strategy. Fine details can be manufactured even on thin-walled components or in sections with problematic heat dissipation [34].

In relation to the current state of the art, numerous papers focus on WAAM manufacturing of Inconel alloys. Most papers address Inconel 718 (IN718) alloy, and only [26, 28, 38, 42–44] focus on Inconel 625. WAAM components from Inconel 718 require post-process heat treatment [9], which is no obstacle for manufacturing blank parts. According to [9, 36], Inconel 625 (IN625) does not require post-process heat treatment. This property makes IN625 more suitable for hybrid WAAM [37] of a finished component in one machine. Analysis of material properties is a common step in the process of developing a technology strategy. Analysis enables an understanding of the elementary principles of the manufacturing process. To develop a reliable manufacturing method, it is necessary to study the material properties of

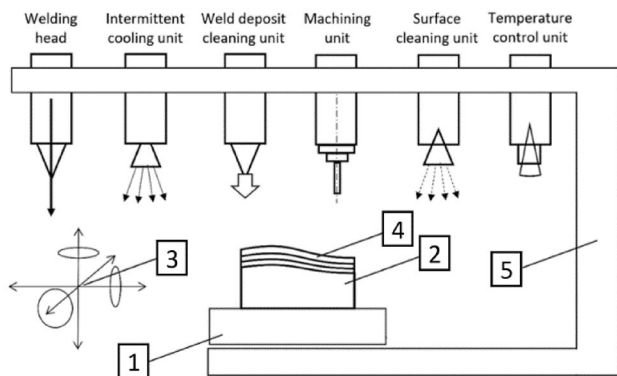


Fig. 1 WAAM method for building parts. 1, machine tool table with inner cooling; 2, basic material; 3, machine tool coordinate system; 4, welded material; 5, frame of the machine tool

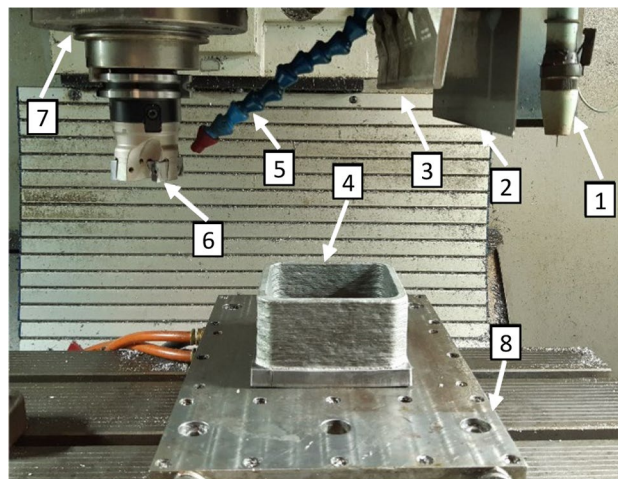


Fig. 2 Experimental machine workspace. 1, welding torch; 2, welding process shielding; 3, air blade pressure cleaning; 4, manufactured part; 5, milling process cooling; 6, milling tool; 7, spindle; 8, worktable with inner cooling

samples manufactured using various complementary operations and methods.

Study [42] focused on comparison of the material properties of a standard CMT continuous WAAM process and a CMT WAAM process with pulsed droplet transfer during the manufacturing of IN625. Both techniques demonstrated YS and UTS results that were about 20% better than a casted sample. The CMT WAAM with pulsed droplet transfer manufactured sample was even slightly better (5 to 15%) than the standard CMT continuous WAAM samples in YS, UTS and hardness. There are similarities between CMT WAAM process with pulsed droplet transfer and CMT discontinuous WAAM. In pulsed droplet transfer, the welding variables oscillate in a defined range. Similarly, in CMT discontinuous WAAM, the welding variables oscillate from zeros to a defined values. However, the frequency is different. Investigation of the material properties of an IN625 manufactured

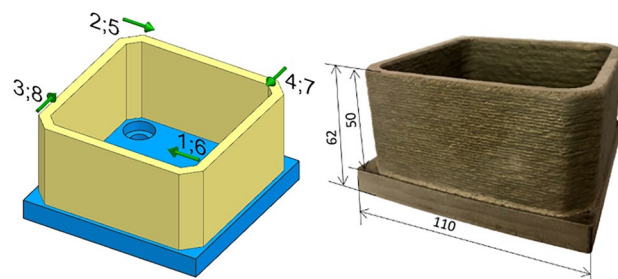


Fig. 3 Scheme of chronological order of weld cladding starts and directions (left), dimensions of manufactured samples (right)

Table 4 Welding parameters

CMT continuous WAAM — A samples		CMT discontinuous WAAM — B samples	
Wire feed [m/min]	7.1	Wire feed [m/min]	8.1
Torch travel speed [m/min]	0.5	CMT parameter (droplets) [-]	-2.5
Current [A]	100	Pitch distance of spots [mm]	3.0
Voltage [V]	14.8	Current [A]	186
Shielding gas flow [l/min]	15	Voltage [V]	14.6
		Shielding gas flow [l/min]	13

using CMT discontinuous WAAM can further confirm or contradict the results from [42].

For the CMT WAAM process of IN625, a special gas mixture designed for nickel based super alloys was chosen as a shielding gas. This gas mixture is recommended by the Messer Group GmbH [41]. Furthermore, the studies [39, 40] are mentioning the importance of having a helium proportion of about 20–25% in the shielding gas mixture.

Standard analytical tools in contemporary research include optical microstructure and macrostructure analysis, hardness analysis and SEM analysis. Many studies also rely on tensile strength testing and EDS analysis. To keep the present research relevant to the current state of the art, all of these standard types of analyses were performed. It is clear that the properties of Inconel 625 alloy, which should retain its tensile strength at elevated temperatures, make a tensile strength test at 650 °C [6] very relevant for this research.

The main goal of this paper is to expand the state of the art in WAAM of Inconel 625. CMT discontinuous WAAM strategy which is known technology [35], but not yet used in WAAM of Inconel 625 according to current state of art. CMT discontinuous WAAM will be tested and compared with a standard CMT WAAM. Complex material analyses will be performed, including metallography, SEM (scanning electron microscope), x-ray tomography, hardness, wear resistance and tensile strength. The last two material properties will be investigated at room temperature (20 °C) and also at an elevated temperature of 650 °C [45].

2 Materials, experimental procedure and methods

2.1 Materials and shielding gas

To implement the experiment, it was necessary to define and obtain welding and substrate material along with shielding gas. The essential materials used in the experiments are specified in the tables below (Tables 1, 2 and 3).

Thermanit welding wire Ø 1 mm from Voestalpine Böhler Welding GmbH was used as an input material. The chemical composition and elementary mechanical properties of the wire are shown in Table 1.

Steel plates were selected as a substrate material. It was found [40] that welding Inconel 625 on weldable carbon steel is suitable. Plates made of EN—S235 JRG 1 according to EN 10,025 were prepared for the following dimensions: steel plate 110 × 110 × 12 mm. The chemical composition and elementary mechanical properties of the plates are depicted in Table 2.

The shielding gas is a mixture designed by Messer Group GmbH for welding nickel-based alloys. The composition of the shielding gas mixture is provided in Table 3. The gas flow is controlled by the flow valve to a level of 13 or 15 l/min depending on the WAAM strategy. Although [38] presents testing of different gasses, the experiments implemented for the present paper rely on recommendations by Messer welding experts with industrial experience. The

Table 5 Auxiliary technological data

Layer height (continuous)	1.2 mm	Layer height (discontinuous)	1.7 mm
Milling tool	Walter F4041 B22.050.Z04	Milling inserts	Iscar H490 ANKX 120508PNTR
Cutting speed	50 m/min	Feed per tooth	0.2 mm/tooth

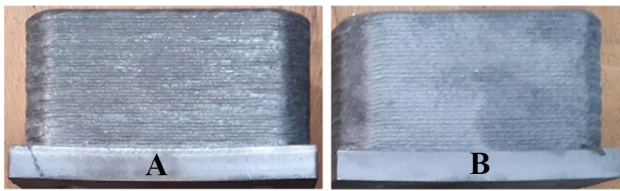


Fig. 4 Detail of manufactured samples: type **A** wall structure, continuous WAAM (left); type **B** wall structure, discontinuous WAAM (right)

presence of helium in the mixture also aligns with research papers [39, 40].

2.2 Experimental procedure, strategy and samples

An innovative patented hybrid manufacturing method using WAAM was used for the metal deposition process. This method utilizes a welding unit as a part of a 3-axis vertical CNC milling centre. The welding torch is in the same workspace as the milling spindle. The hybrid manufacturing method is characterized by this sequence of operations [37]: (i) deposition of a metal layer using electric arc welding in a protective atmosphere, (ii) machining aimed at creating a geometrically defined surface for another weld deposit, (iii) mechanical surface cleaning and (iv) air cooling/cleaning. At the cost of slightly reduced productivity, WAAM on a defined machined surface greatly increases the manufactured part's precision and possible shape complexity. Inter-operational cleaning also reduces porosity and the probability of internal material defects [37]. The method was also used in a study for welding stainless steel [46] (Fig. 1).

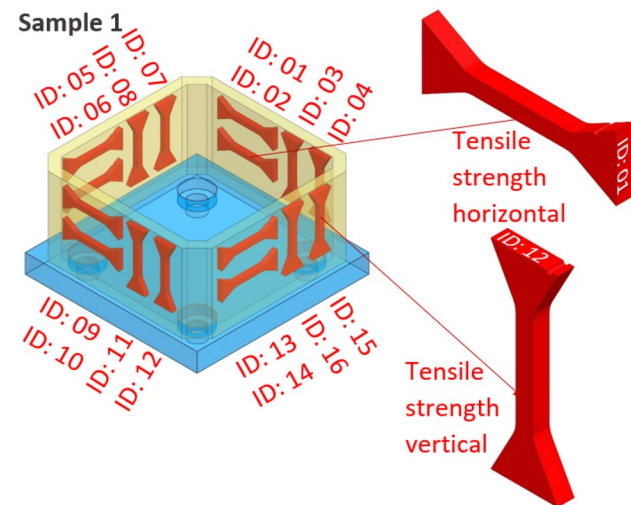


Fig. 5 Specimen layout in sample 1

The experiments were performed on a 3-axis CNC hybrid machine. A Bridgeport VMC 500 XP vertical machining centre with a Heidenhain iTNC 530 control system was combined with a Fronius CMT Advanced 4000R welding unit. A Fronius Robacta Drive CMT W pro welding torch was positioned parallel to the milling spindle. Other accessories required for hybrid WAAM technology (wire feeder, air cleaning/cooling, water cooled table) were incorporated into the machine setup (Fig. 2).

The experimental samples were manufactured using the welding parameters presented in Table 4. The layers were manufactured one after another in the manner shown in Fig. 3, where weld cladding starts and directions are described. The size of the shape is approximately 110×110 mm with a height of 50 mm from the 12-mm-thick substrate. For both of the welding strategies described in Tables 4 and 5, two identical samples were manufactured, resulting in a total of four samples. Wall structure detail of these samples is shown in the Fig. 4. The welding parameters were optimized during the preceding research through visual inspection only. The material properties were unknown, and therefore, performing material tests is an overall advancement in WAAM technology research at the CTU.

The specimens for the material tests were extracted from samples using an EDM (electrical discharge machining) process. The layout of all specimens is shown in Figs. 5 and 6.

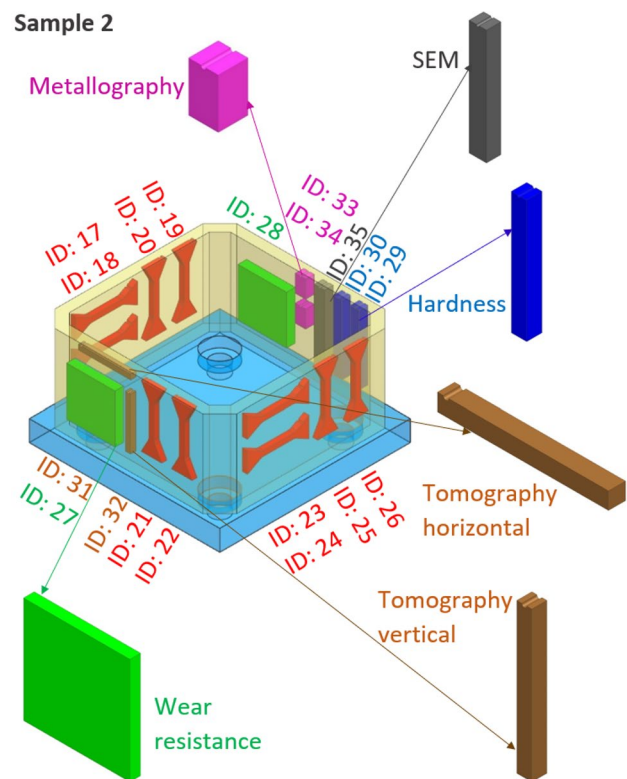


Fig. 6 Specimen layout in sample 2

Table 6 List of material tests**Structural**

Analysis of metallographic specimen (metallography)
 Analysis of morphology and element composition (scanning electron microscope, SEM)
 Defect volume and pores inspection (X-ray tomography)

Mechanical

Hardness of the machined surface (Vickers)
 Wear resistance of the machine surface (20 °C and 650 °C) – pin-on-disc
 Tensile strength (20 °C and 650 °C)

There are two types of tensile specimens: (i) horizontal and (ii) vertical.

2.3 Analytical methods

To analyse the material properties of the manufactured samples, the material tests shown in Table 6 were performed. These tests are divided into structural tests and mechanical tests:

(i) Metallography (specimens 33A, 33B, 34A, 34B).

The microstructure of the specimens was revealed by electrolytic etching in an electrolyte consisting of a 10% aqueous solution of oxalic acid with a Struers Polipower DC source with the following setup: 2.5 V, 20 s. The microstructure was then observed using a Carl Zeiss Jena Neophot 32 light optical microscope.

(ii) SEM (specimens 35A, 35B).

A Jeol JSM-7600F SEM microscope equipped with an EDS detector and EBSD detector was used to make observations. The acceleration voltage was 15 kV. Images

were taken with a LEI detector (secondary electrons) and LBE detector (back scattered electrons). The secondary electrons provide information about the structure and morphology of the observed sample. The back scattered electrons slightly reflect the chemical composition of the observed sample.

(iii) X-ray tomography (specimens 31A, 31B, 32A, 32B).

X-ray tomography was conducted using a Zeiss Metrotom 1500 system with a 225 kV and 2 K detector with a pixel size of 0.2 mm. Samples with a square cross-section of 3 × 3 mm were selected to obtain high-resolution images of the scanned point cloud. The CT system settings for the tested samples were acceleration voltage of 225 kV, with a current of 460 μA, integration time of 600 ms with activated image averaging from 3 pictures in each angular position for noise reduction and a 2 mm copper filter to adjust the X-ray spectrum to eliminate beam hardening artefacts to obtain the best imaging. Magnification of 8.8 × led to a final voxel size of 0.0227 mm. The porosity analysis was evaluated using VG Max software with an EasyPore algorithm; all pores bigger than 8 voxels were considered in the statistics, which is a common rule to

Fig. 7 Macrostructure comparison of **A**, CMT continuous WAAM (left), and **B**, CMT discontinuous WAAM (right), specimens

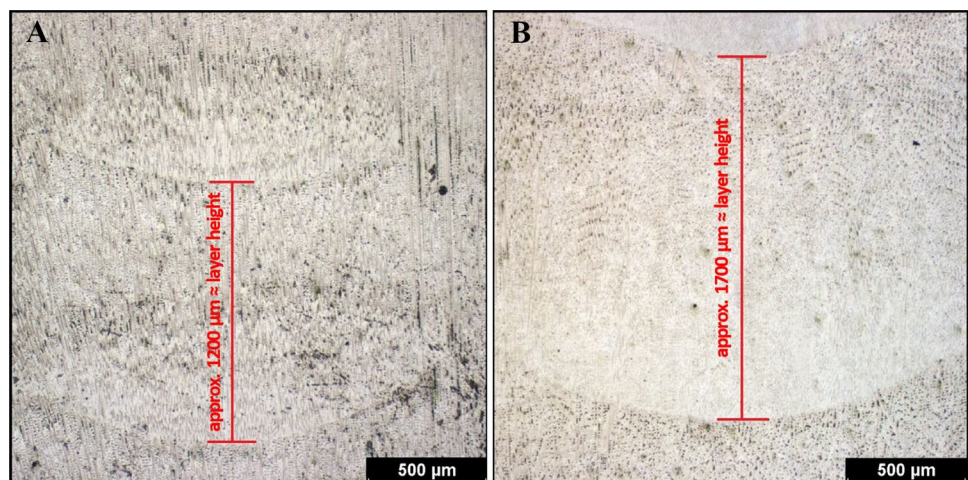
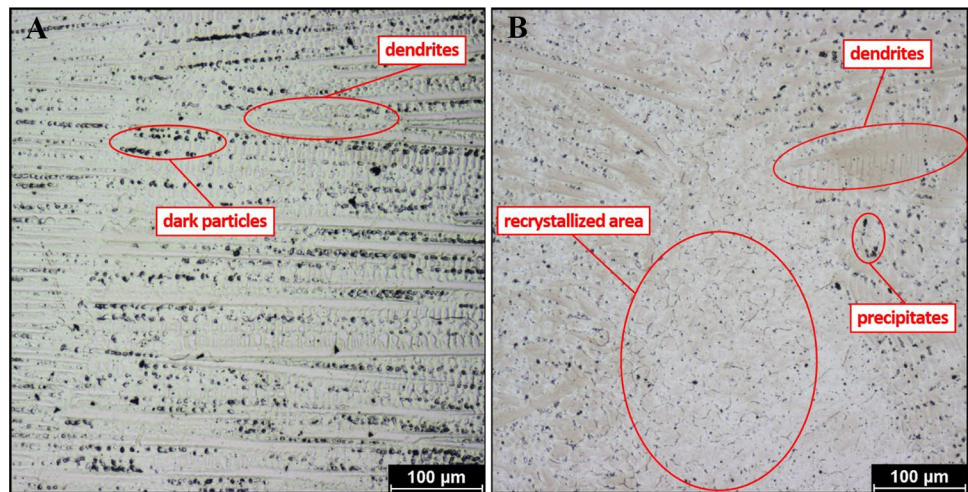


Fig. 8 Detailed structural comparison of **A**, CMT continuous WAAM (left), and **B**, CMT discontinuous WAAM (right), specimens



exclude image noise from the evaluation. Each sample scan contained more than 700 million voxels.

(iv) Hardness (specimens 29A, 29B).

The Vickers hardness (load 10 kg, HV10) of the specimens was measured using a Struers Duramin 40-AC3 universal hardness testing machine.

(v) Wear resistance (specimens 27A, 27B).

Dry sliding tribological tests were carried out on the specimens (ground with water-cooled 800 grit SiC paper) at 20 °C and 650 °C using an Anton Paar THT-S-CE 0000 pin-on-disc tribometer. The static friction partner was an

Al₂O₃ ball with a diameter of 6 mm. The test parameters were: wear track radius 3 mm, normal force 5 N and linear speed of the revolving partner 5 cm/s with a stop condition of 5000 laps. The relative humidity in the laboratory was 37%. The results of the pin-on-disc testing (i.e. profiles of wear track on both the ball and the revolving friction partner) were evaluated using an Olympus DSX1000 light optical microscope.

(vi) Tensile strength (specimens 1-20A, 1-20B).

An Instron 3369 machine was used for the measurements. The crosshead speed was 2.4 mm/min. All the tests were performed according to the EN ISO 6892-1:2009 standard. Five measured specimens were used for each set.

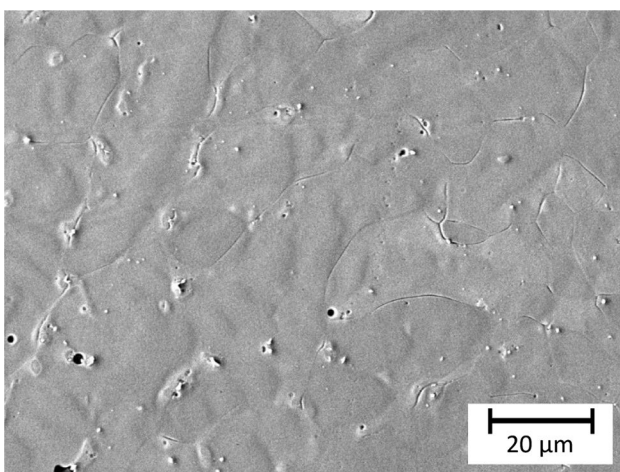


Fig. 9 Detail of the partially recrystallized grains (33B)

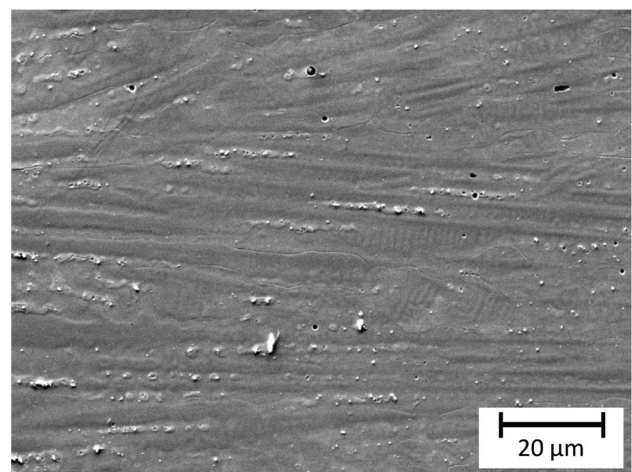
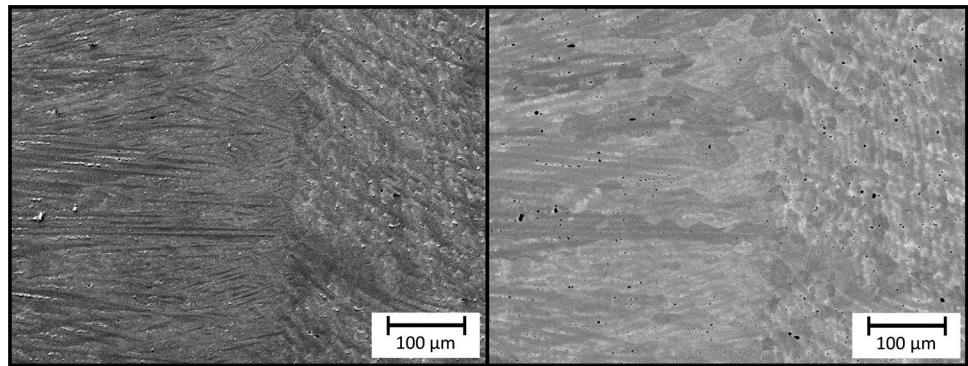


Fig. 10 Detail of the dendritic structure (33B)

Fig. 11 Comparison of secondary and back scattered electron images (33B)



3 Results and discussion

3.1 Analysis of metallographic specimen

Micrographs of the etched 33A, 33B, 34A and 34B specimens obtained by LOM showed the presence of the layers characteristic for the additive manufacturing technologies as well as molten pool boundaries (MPBs). The microstructure is coarser closer to the boundaries of these layers, where it can act as a crack nucleation site. The observed areas are significant with the dendritic structure in the same direction. However, the microstructure is not cellular as in the case of 3D printing technologies, but is more reminiscent of the welded/clad microstructure. This can be seen in Fig. 7.

The boundaries of the dendrites are rich with dark particles (Fig. 8); depending on the chemical composition of

the filler wire, these may be Nb-, Mo- or Ti-rich carbides. Further investigation was conducted using SEM.

In the CMT discontinuous WAAM samples (B), there are areas with polyhedral grains, which imply partial recrystallization (see Fig. 8). This leads to the conclusion that, in the B setup, the energy input was insufficient for partial recrystallization. The structure of the CMT discontinuous WAAM samples (B) is more inhomogeneous but also more fine-grained than the structure of the CMT continuous WAAM samples (A). A more fine-grained structure could indicate better mechanical properties. These mechanical properties will be further investigated.

There was no observable structural difference between specimens 33A and 34A or between specimens 33B and 34B. Thus, no structural difference was observed along the layer building direction for either of the WAAM strategies.

Fig. 12 Chemical composition maps (33B)

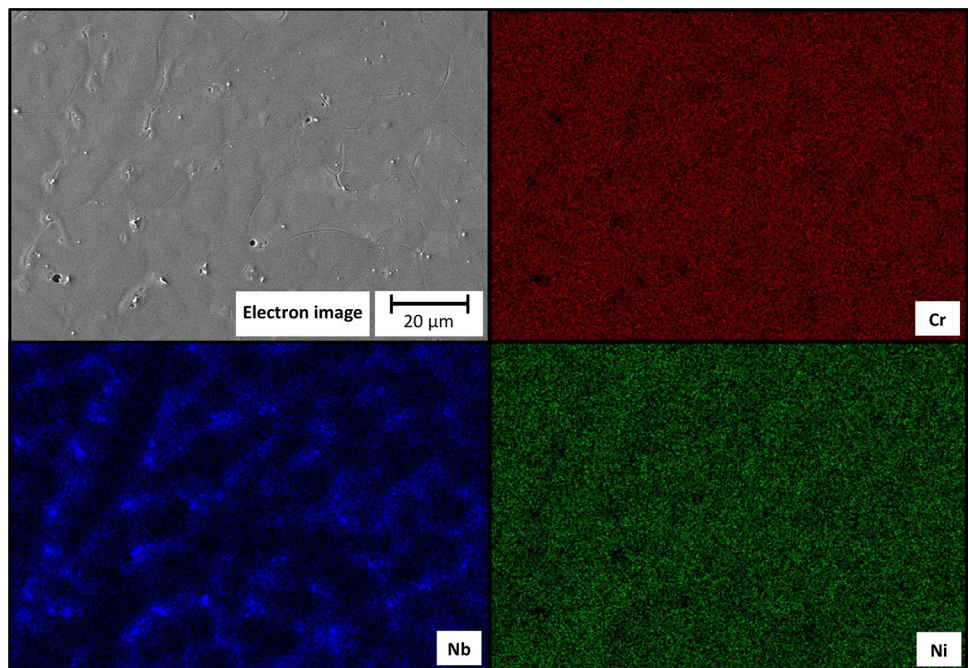
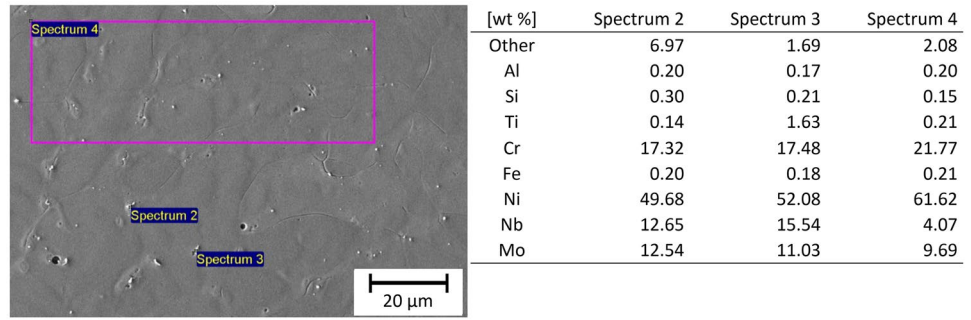


Fig. 13 EDXS measurement (33B)



3.2 Analysis of morphology and element composition

Scanning electron microscopy (SEM) did not show any notable differences between WAAM strategies A and B or any notable differences along the layer building direction. The scanning electron microscopy observations were mainly focused on documenting the particles located at the recrystallized grain boundaries and dendrite boundaries.

The chemical composition analysis of the particles was performed via EDXS analysis.

The two micrographs shown below (Figs. 9 and 10) document the microstructure of partially recrystallized grains and dendritic structure in specimen 33B. These two microstructural states are regularly repeated with respect of the clad 3D printed layers and their thermal influence on each other.

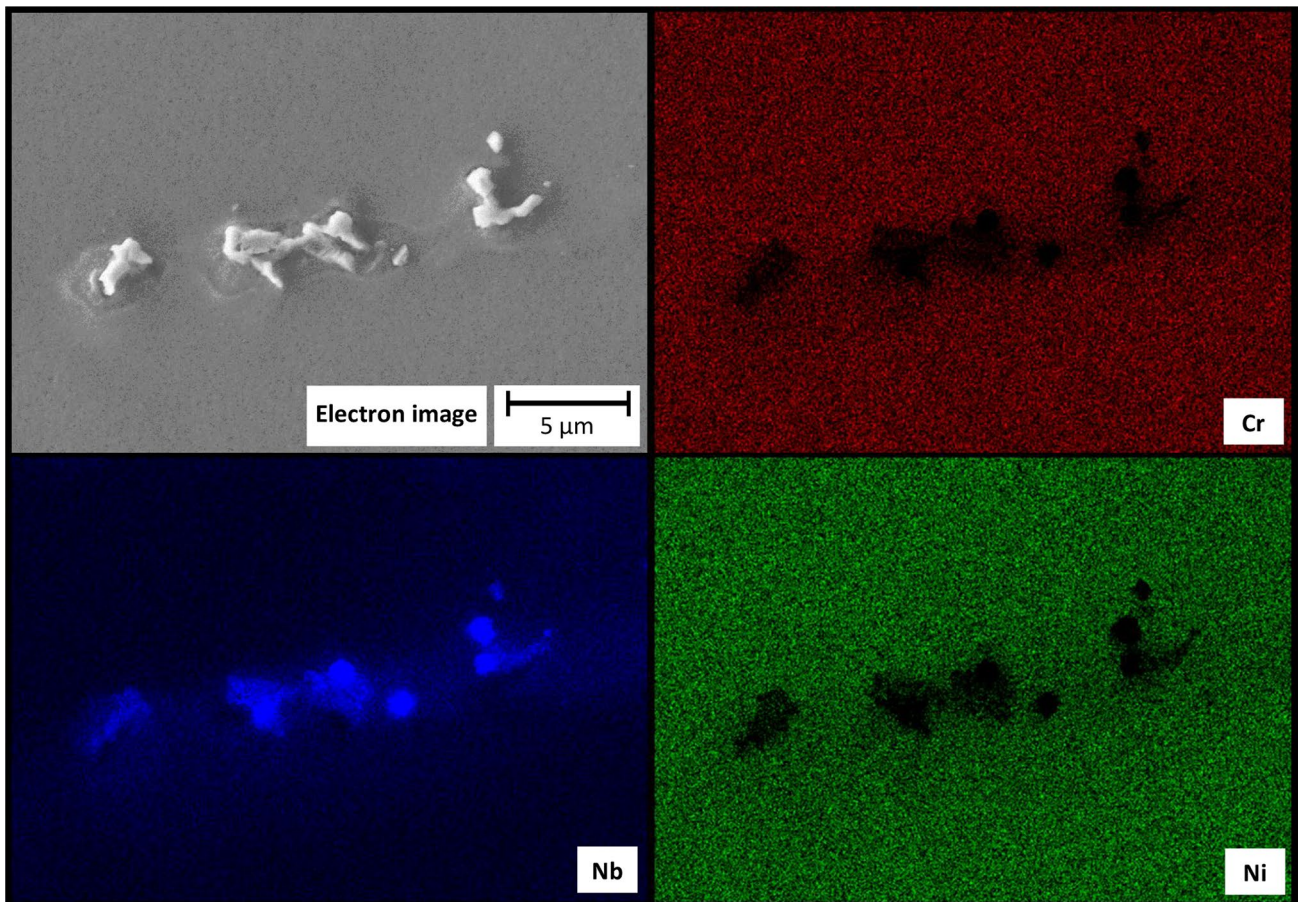
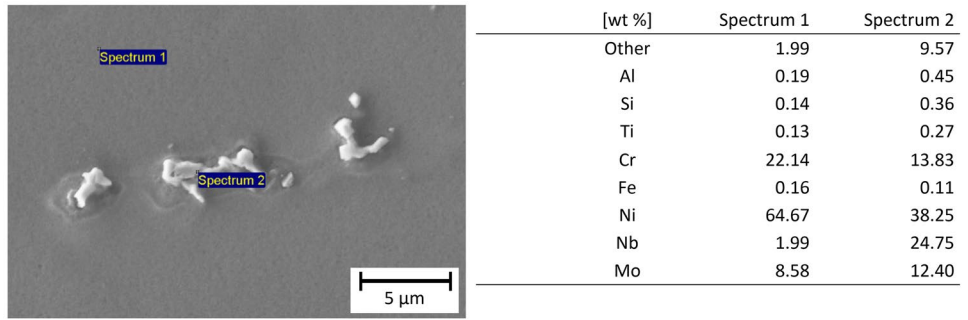


Fig. 14 Chemical maps of precipitated particles (33B)

Fig. 15 Detailed EDXS measurement (33B)



The micrographs below document the morphology and chemical composition of the clad layers (Fig. 11). Oriented dendritic grains, which grow from partially recrystallized grains with particles at their grain boundaries, are visible. This type of microstructure corresponds with layer cladding and heat involving the previous layer.

Chemical composition map measurements (Fig. 12) confirmed the homogeneity of the 3D printed samples, with segregation of niobium and precipitation of niobium-rich phases. The chemical maps at lower magnification are listed below.

Chemical composition measurements were taken at the same measurement spot. Spectrum 4 represents the global chemical composition, and spectrum 2 and 3 correspond with the niobium base particles. The results of the EDXS measurements are shown in Fig. 13.

The global chemical composition corresponds with the filler metal used for 3D printing. The measured chemical composition in spectrum 2 and 3 confirms the higher niobium content, but the particles are small. The surrounding base material was involved in the measurements and affected the results.

EDXS measurements of the chemical composition for the precipitated particles were taken using higher magnification. The chemical composition maps are summarized in Fig. 14.

The measurement of the chemical composition of the niobium part is shown in Fig. 15. The chemical composition led to the result that the particle is niobium carbide with a niobium content of over 24 wt %.

3.3 Defect volume and pores inspection

The basic statistics and visualizations generated for all samples and results from the porosity analysis are summed up in Fig. 16.

Figure 16 indicates that there is a significant difference between the pore count and size on samples made by CMT continuous WAAM and those made CMT discontinuous WAAM. The largest pore detected among all of the samples was recorded on sample 31B (horizontal sample made by spot welding), which had a volume of $7.3 \times 10^{-3} \text{ mm}^3$, which is 619 voxels in total (Fig. 16). The smallest pore size and the only pore detected in the entirety of specimen 32A had a pore volume of $9.0 \times 10^{-5} \text{ mm}^3$ in a total of 8 voxels. This is the smallest pore size that may be practically detected by the given CT system and parameter settings for the specific material and sample size.

Porosity was evaluated as a defect volume ratio; in other words, the ratio between total material volume and total defect volume, both calculated in mm^3 . The porosity analysis results are described in Table 7.

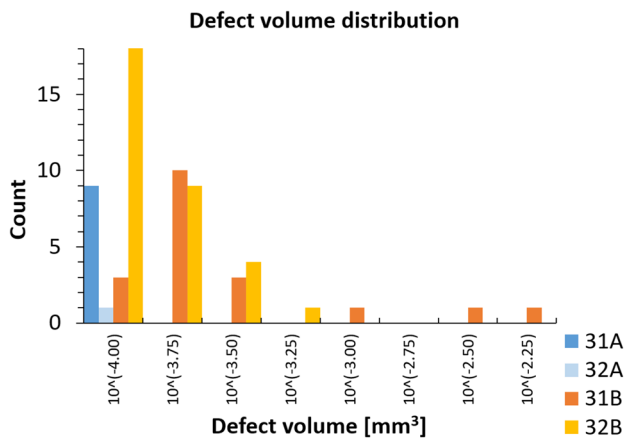


Fig. 16 Porosity analysis on samples: histogram of defect sizes and frequencies

Table 7 Porosity analysis results

Sample	Material volume [mm^3]	Defect volume [mm^3]	Defect volume ratio [%]	Total pores detected
31A	270.15213	0.00099	0.00036	9
31B	268.44717	0.01568	0.00584	19
32A	270.15582	0.00009	0.00003	1
32B	270.49005	0.00544	0.00201	33

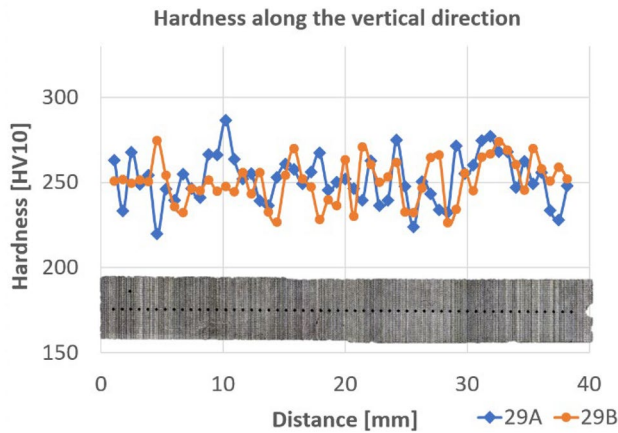


Fig. 17 HV10 hardness along samples 29A and 29B

Both of the CMT continuous WAAM samples had significantly lower porosity than the CMT discontinuous WAAM samples. The largest pore detected on a CMT continuous WAAM sample was detected on sample 31A with a volume of $1.3 \times 10^{-4} \text{ mm}^3$ and 11 voxels. The largest and the only pore detected on sample 32A was a pore with a volume of $9.0 \times 10^{-5} \text{ mm}^3$ in a total of 8 voxels. The largest pore detected from all of the samples was recorded on sample 31B (horizontal sample made by CMT discontinuous WAAM) with a volume of $7.3 \times 10^{-3} \text{ mm}^3$ which is 619 voxels in total. The largest pore detected on vertical sample 32B made by CMT discontinuous WAAM had a volume of $4.7 \times 10^{-4} \text{ mm}^3$ with 40 voxels in total.

3.4 Hardness of the machined surface

The hardness measurement was carried out on specimens 29A and 29B. The measurement layout along with the results is presented by the graph in Fig. 17. The average

hardness of specimen 29A is $252 \pm 14 \text{ HV}_{10}$, and the average hardness of specimen 29B is $251 \pm 13 \text{ HV}_{10}$. Based on these results, there is no hardness variance between sets A and B. The scatter of the hardness values along the x-axis corresponds with the heterogeneous microstructure after the manufacturing process.

3.5 Wear resistance of the machined surface

The results of the pin-on-disc test were evaluated as the volume loss in cubic millimetres for both the pin and the disc. The wear profile of the pin and disc was measured using optical microscopy profiling in the Z-axis and then calculated by approximative equations given in the standard ASTM G99-5 [47]. The profile of the wear tracks and loss area were then calculated as the volume loss (see Fig. 18). The dynamic coefficient of friction was recorded during the test. The significant difference between the 20 and 650 °C tests can be seen (Fig. 19) in the dynamic friction coefficient and also in the volume loss of the disc. The ball wear was approximately the same in all four cases, while the volume loss at 20 °C and 650 °C on the side of the disc is two to three times higher than by the static friction partner.

The dry sliding dynamic friction coefficient (see records in Fig. 19) in the room temperature test fluctuated around an average of 0.75. Significant peaks up to 0.9 can be seen in the middle of the total time. This may be caused by an uneven microstructure with the particles causing a ploughing effect. In the case of the elevated temperature test at 650 °C, the friction coefficient was stable at 0.15–0.2.

This can lead to the conclusion that this alloy performs better at higher temperatures. Nevertheless, the wear track and wear mechanisms are different (oxidation and adhesion at elevated temperature) and must be considered in future product design. The cross-section of the wear track and its

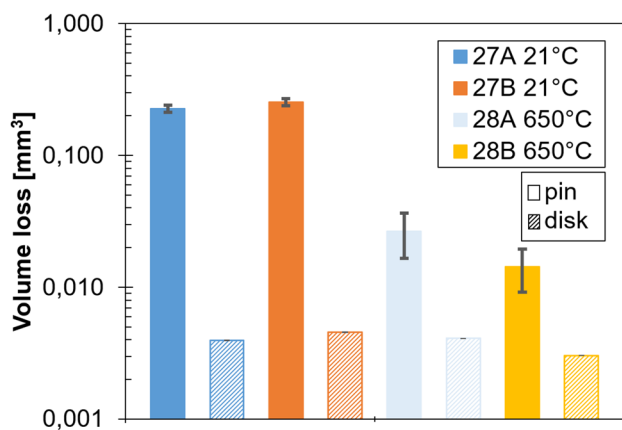


Fig. 18 Volume loss of the static and revolving friction partners after the pin-on-disc test

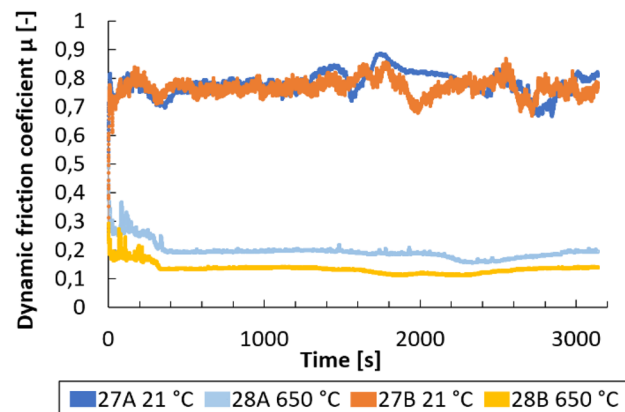


Fig. 19 Dynamic friction coefficient during the pin-on-disc test at 21 and 650 °C

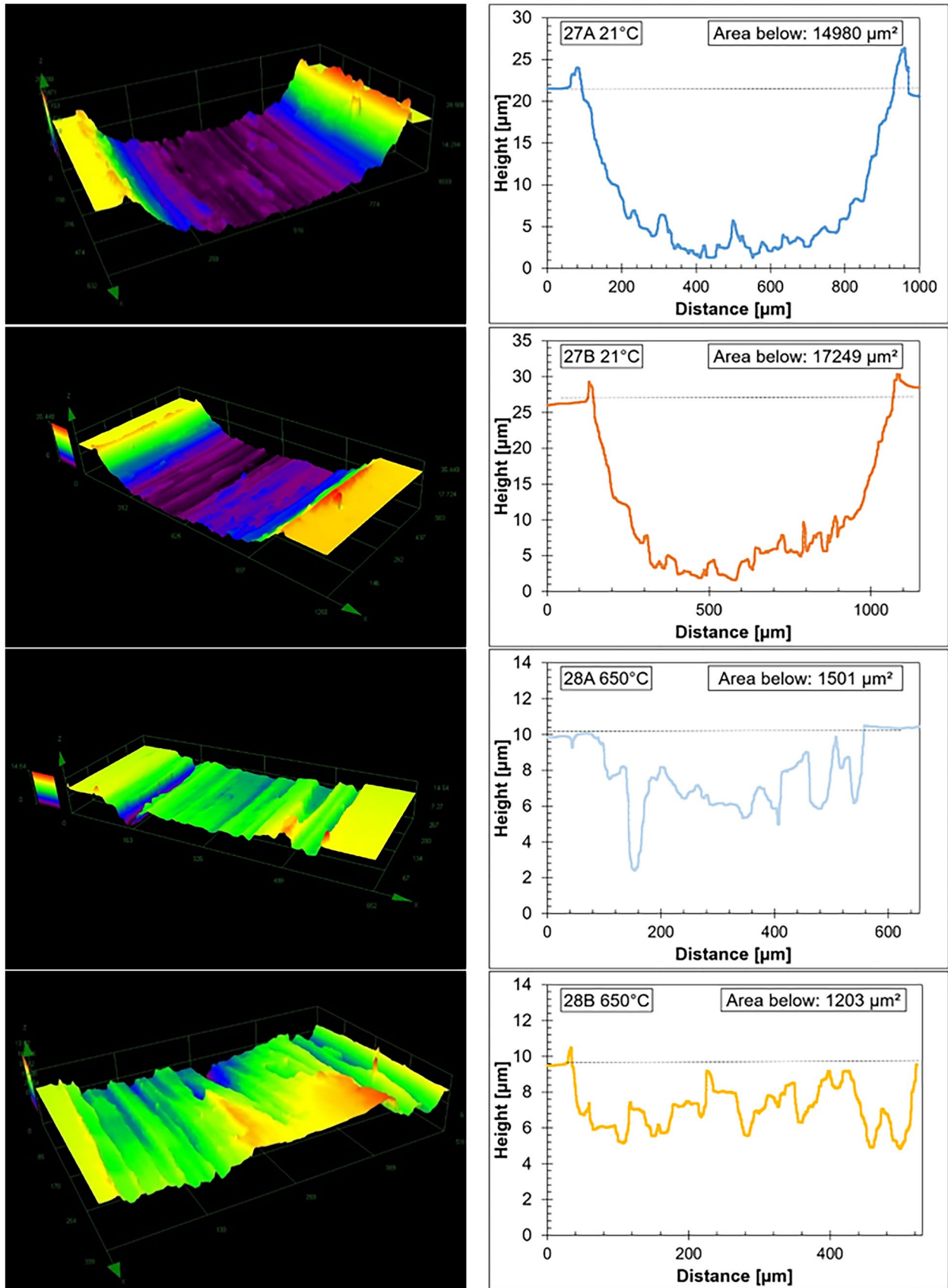


Fig. 20 Profiles of specimen wear tracks



Fig. 21 Tensile testing: example photography of ruptured specimen (CMT discontinuous WAAM—vertical—20 °C)

3D profiles can be seen in Fig. 20. The wear track after the high temperature test was shallow with a stacked volume in the middle.

3.6 Tensile strength

An example set of ruptured specimen is shown on the Fig. 21. The results of tensile tests at a temperature of 20 °C are shown in Table 8 and Fig. 22. The standard deviations of YS and UTS are small, which corresponds to the excellent homogenous structure of the samples. The standard deviation of elongation values is quite noticeable, which is probably caused by the different position of rupture on the specimen during the tensile test.

For both the CMT continuous WAAM and CMT discontinuous WAAM strategies, the UTS in the horizontal direction is slightly higher than in the vertical direction (2% continuous, 8% discontinuous). This phenomenon does not apply to YS. Overall, the CMT discontinuous WAAM strategy specimen has a YS that is 13% higher in the horizontal direction and 1% lower in the vertical direction than the CMT continuous WAAM strategy specimen. Similarly, the UTS of the CMT discontinuous WAAM strategy specimen is 20% higher in the horizontal direction and 13% higher in the vertical direction than of the CMT continuous WAAM strategy specimen.

Table 9 and Fig. 23 show the results of tensile tests of WAAM samples of Inconel 625 at a temperature of 650 °C. Deviations for YS and UTS are similarly small, which corresponds to the excellent homogenous structure of the samples. Deviations for elongation values are also quite noticeable and are caused by the different position of rupture on the specimen during the tensile test.

Even at 650 °C, the WAAM Inconel 625 retains most of its mechanical properties. However, in comparison with an annealed bar of Inconel 625 [6], the decrease of YS and UTS

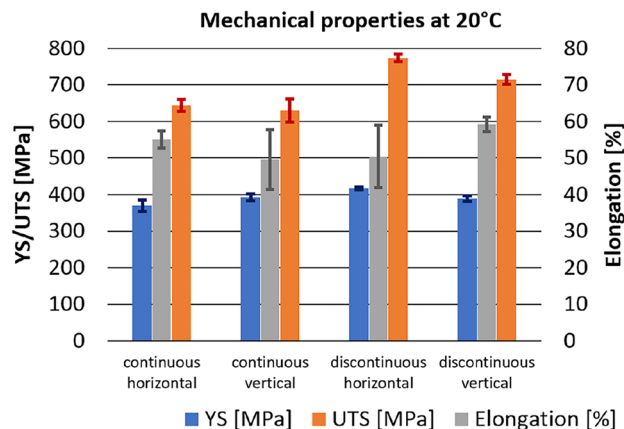


Fig. 22 Mechanical properties of Inconel 625 welds at 20 °C

is more significant. While annealed Inconel 625 at 650 °C has approximately 15% YS and lower UTS compared to its 20 °C values, the CMT discontinuous WAAM specimens show a decrease of approx. 26%, and the CMT continuous WAAM specimens show a decrease of approx. 30% compared to the 20 °C values. The comparison is described in Tables 10 and 11.

The last comparison pertains to the published tensile strength results of WAAM Inconel 625; see Table 12. Both the CMT continuous WAAM and CMT discontinuous WAAM specimens have the highest YS of the published results. The UTS of the CMT discontinuous WAAM specimen is also the highest among the published results, while the UTS of the CMT continuous WAAM specimen is slightly below the average.

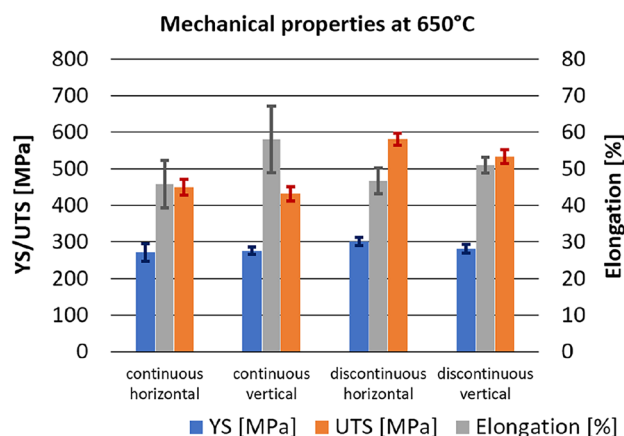


Fig. 23 Mechanical properties of Inconel 625 welds at 650 °C

Table 8 Mechanical properties of Inconel 625 welds at 20 °C

	YS [MPa]	UTS [MPa]	Elongation [%]
CMT continuous WAAM—horizontal	369 ± 16	643 ± 16	55.0 ± 2.3
CMT continuous WAAM—vertical	392 ± 10	630 ± 31	49.6 ± 8.2
CMT discontinuous WAAM—horizontal	417 ± 4	773 ± 10	50.4 ± 8.5
CMT discontinuous WAAM—vertical	389 ± 8	715 ± 13	59.2 ± 2.0

Table 9 Mechanical properties of Inconel 625 welds at 650 °C

	YS [MPa]	UTS [MPa]	Elongation [%]
CMT continuous WAAM—horizontal	271 ± 24	450 ± 22	45.8 ± 6.5
CMT continuous WAAM—vertical	276 ± 10	432 ± 20	58.0 ± 9.1
CMT discontinuous WAAM—horizontal	301 ± 11	581 ± 17	46.7 ± 3.5
CMT discontinuous WAAM—vertical	282 ± 12	534 ± 19	51.0 ± 2.2

Table 10 Mechanical properties of Inconel 625 welds: comparison at 20 °C and 650 °C (vertical direction)

	20 °C		650 °C		YS decrease [–]	UTS decrease [–]
	YS [MPa]	UTS [MPa]	YS [MPa]	UTS [MPa]		
Annealed [6]	492	965	419	812	15%	16%
CMT continuous WAAM	392 ± 10	630 ± 31	276 ± 10	432 ± 20	30%	31%
CMT discontinuous WAAM	389 ± 8	715 ± 13	282 ± 12	534 ± 19	28%	25%

Table 11 Mechanical properties of Inconel 625 welds: comparison at 20 °C and 650 °C (horizontal direction)

	20 °C		650 °C		YS decrease [–]	UTS decrease [–]
	YS [MPa]	UTS [MPa]	YS [MPa]	UTS [MPa]		
Annealed [6]	492	965	419	812	15%	16%
CMT continuous WAAM	369 ± 16	643 ± 16	271 ± 24	450 ± 22	27%	30%
CMT discontinuous WAAM	417 ± 8	773 ± 13	301 ± 11	581 ± 17	28%	25%

Table 12 Comparison of published results at 20 °C (vertical direction)

	YS difference [–]	UTS difference [–]	Elongation difference [–]
CMT continuous WAAM	Reference	Reference	Reference
CMT discontinuous WAAM	– 1%	+ 13%	+ 19%
Torch speed 0.48 m/min [26]	– 4%	+ 3%	– 6%
Torch speed 0.54 m/min [26]	0%	+ 7%	– 10%
Torch speed 0.60 m/min [26]	+ 2%	+ 9%	– 13%
Weave torch trajectory [28]	-	+ 2%	+ 21%
Multiple clads [28]	-	+ 8%	+ 19%
Shielding gas 2.5% CO ₂ [38]	+ 11%	+ 19%	-
Sh. gas 3% He, 1.5% H ₂ [38]	– 10%	+ 11%	-
Shielding gas 5% H ₂ [38]	– 20%	+ 11%	-
Shielding gas 99.999% Ar [38]	– 14%	+ 11%	-
As deposited [44]	– 5%	+ 4%	+ 13%
30 min heat-treated [44]	– 7%	+ 6%	– 3%
1-h heat-treated [44]	– 8%	+ 7%	– 13%
2-h heat-treated [44]	+ 1%	+ 9%	– 7%
CMT continuous WAAM with short arc droplet transfer [42]	– 35%	– 8%	+ 31%
CMT continuous WAAM with pulsed droplet transfer [42]	– 28%	– 6%	+ 33%

4 Conclusions

The aim of this study was to analyse the material properties of an innovative CMT discontinuous WAAM strategy used for Inconel 625 material. The CMT discontinuous WAAM strategy is suitable for building complex shapes, fine details and thin-walled components, mainly due to the lower heat input. The results of this innovative WAAM strategy were compared to the standard CMT continuous WAAM strategy performed by the authors of the study and also to published results pertaining to WAAM of Inconel 625. The material analysis demonstrated that the CMT discontinuous WAAM strategy has the following benefits and differences.

1. Metallography showed that the structure of the samples is quite similar to the welded/clad structure. This was expected given the character of WAAM technology. The CMT discontinuous WAAM strategy samples were affected by partial grain recrystallization, and their structure is more fine-grained. Thus, the microstructure of the CMT discontinuous WAAM strategy samples is more inhomogeneous than the CMT continuous WAAM strategy samples.
2. SEM was used to analyse the details of the microstructure. No element composition difference was observed between the CMT continuous (A) and CMT discontinuous (B) WAAM strategies. The element composition corresponds to the Thermanit 625 filler wire that was used. The presence of precipitated niobium particles was confirmed. These particles were quite small (2–5 µm). The chemical composition led to the result that the particle is niobium carbide with a niobium content of over 24 wt %.
3. X-ray tomography proved that there were no significant internal defects in the manufactured structure of either the CMT continuous WAAM strategy or the CMT discontinuous WAAM strategy samples. It is reasonable to say that the pores detected on the CMT continuous WAAM strategy samples were fewer in total and much smaller in size than the pores on the CMT discontinuous WAAM strategy samples. On the other hand, all defect volume ratios are on a very small scale compared to the total volume of material. Even the largest porosity of 0.00584% is a very good result compared to, for example, PBF-LB technology, where the lowest porosity detected with the same technology was in the range of 0.02%, where other researchers achieve the lowest levels of porosity in the range of 0.8% with PBF using metallography analysis [48].
4. Based on the hardness measurement results, there is no hardness variance between the CMT continuous WAAM strategy and CMT discontinuous WAAM strategy samples. The scatter of the hardness values along the layer

building direction corresponds with the heterogeneous microstructure after the manufacturing process.

5. Wear resistance measurements lead to the conclusion that this alloy performs better at higher temperatures. Nevertheless, the wear track and wear mechanisms are different (oxidation and adhesion at elevated temperature) and must be considered in future product design. The CMT discontinuous WAAM strategy samples performed even better at an elevated temperature of 650 °C, as the volume of its wear was about half of that of the CMT continuous WAAM strategy samples.
6. Tensile strength test results clearly show that the tensile mechanical properties of the CMT discontinuous WAAM strategy specimens are better than those of the CMT continuous WAAM strategy specimens. The YS is similar for both strategies, but the UTS of the CMT discontinuous WAAM specimens is approx. 15% higher at 20 °C, and the retention of the mechanical properties (YS and UTS) at a temperature of 650 °C is approx. 4% better. The CMT discontinuous WAAM strategy achieved the second highest UTS amongst the published results of Inconel 625 clads.

Acknowledgements The authors would like to express their thanks for the support provided by ESIF, EU Operational Programme Research, Development and Education.

Author contribution Not applicable.

Funding This study is supported by the EU Operational Programme Research, Development and Education and the Center of Advanced Aerospace Technology (CZ.02.1.01/0.0/0.0/16_019/0000826), Faculty of Mechanical Engineering, Czech Technical University in Prague.

Availability of data and material The authors confirm that the data and material supporting the findings of this work are available within the article.

Declarations

Ethics approval The article follows the guidelines of the Committee on Publication Ethics (COPE) and involves no studies on human or animal subjects.

Consent to participate Not applicable. The article involves no studies on humans.

Consent for publication Not applicable. The article involves no studies on humans.

Competing interests The authors declare no competing interests.

Open Access This article is licensed under a Creative Commons Attribution 4.0 International License, which permits use, sharing, adaptation, distribution and reproduction in any medium or format, as long

as you give appropriate credit to the original author(s) and the source, provide a link to the Creative Commons licence, and indicate if changes were made. The images or other third party material in this article are included in the article's Creative Commons licence, unless indicated otherwise in a credit line to the material. If material is not included in the article's Creative Commons licence and your intended use is not permitted by statutory regulation or exceeds the permitted use, you will need to obtain permission directly from the copyright holder. To view a copy of this licence, visit <http://creativecommons.org/licenses/by/4.0/>.

References

1. Ezugwu EO, Bonney J, Yamane Y (2003) An overview of the machinability of aeroengine alloys. *J Mater Process Technol* Volume 134, Issue 2, Pages 233–253, ISSN 0924–0136. [https://doi.org/10.1016/S0924-0136\(02\)01042-7](https://doi.org/10.1016/S0924-0136(02)01042-7)
2. Thellaputta GR, Chandra PS, Rao CSP (2017) Machinability of nickel based superalloys: a review, *Materials Today: Proceedings*, Volume 4, Issue 2, Part A, Pages 3712–3721, ISSN 2214–7853. <https://doi.org/10.1016/j.matpr.2017.02.266>
3. Papavinasam S (2014) Chapter 3 - Materials, Editor(s): Sankara Papavinasam, Corrosion control in the oil and gas industry, Gulf Professional Publishing, Pages 133–177, ISBN 9780123970220. <https://doi.org/10.1016/B978-0-12-397022-0.00003-0>
4. King F (2012) 4 - General corrosion in nuclear reactor components and nuclear waste disposal systems, Editor(s): Damien Féron, In Woodhead Publishing Series in Energy, Nuclear Corrosion Science and Engineering, Woodhead Publishing Pages 77–103, ISBN 9781845697655. <https://doi.org/10.1533/9780857095343.2.77>
5. Choudhury IA, El-Baradie MA (1998) Machinability of nickel-base super alloys: a general review. *J Mater Proc Technol* 77(1–3):278–284 ISSN 0924–0136. [https://doi.org/10.1016/S0924-0136\(97\)00429-9](https://doi.org/10.1016/S0924-0136(97)00429-9)
6. Special Metals Corporation Products, INCONEL® alloy 625, www.specialmetals.com/products
7. Shankar V, Rao KBS, Mannan S (2001) Microstructure and mechanical properties of Inconel 625 superalloy. *J Nucl Mater* 288(2–3):222–232
8. Dinda GP, Dasgupta AK, Mazumder J (2009) Laser aided direct metal deposition of Inconel 625 superalloy: microstructural evolution and thermal stability. *Mater Sci Eng A* 509:98–104
9. Ramkumar KD, Abraham WS, Vijayash V, Arivazhagan N, Rabel AM (2017) Investigations on the microstructure, tensile strength and high temperature corrosion behaviour of Inconel 625 and Inconel 718 dissimilar joints. *J Manuf Process* 25:306–322
10. Yangfan W, Chen Xizhang Su, Chuanchu. (2019) Microstructure and mechanical properties of Inconel 625 fabricated by wire-arc additive manufacturing. *Surf Coat Technol* 374:116–123
11. Alagan NT, Hoier P, Zeman P et al (2019) Effects of high-pressure cooling in the flank and rake faces of WC tool on the tool wear mechanism and process conditions in turning of alloy 718. *Wear* 434–435:102922
12. Alagan NT, Zeman P et al (2019) Investigation of micro-textured cutting tools used for face turning of alloy 718 with high-pressure cooling. *J Manuf Process* 37:606–616
13. Asit Kumar Parida (2018) Kalipada Maity, Comparison the machinability of Inconel 718, Inconel 625 and Monel 400 in hot turning operation. *Eng Sci Technol Int J* 21(3):364–370
14. Li S, Wei Q, Shi Y, Zhu Z, Zhang D (2015) Microstructure characteristics of Inconel 625 superalloy manufactured by selective laser melting. *J Mater Sci Technol* 31:946–952
15. Williams SW, Martina F, Addison AC, Ding J, Pardal G, Colegrove P (2016) *Mater Sci Technol* 32:641

16. Acheson R (1990) Automatic welding apparatus for weld build-up and method of achieving weld build-up; US patent no. (4) 952-769
17. Williams SW, Martina F, Addison AC, Ding J, Pardal G, Colegrove P (2016) Wire + arc additive manufacturing. *Mater Sci Technol* 32(7), 641–647. <https://doi.org/10.1179/1743284715Y.0000000073>
18. <https://www.3dmpwire.com/project-details/goals-and-objectives/>
19. Ding D, Pan Z, Cuiuri D, Li H (2015) Wire-feed additive manufacturing of metal components: technologies, developments and future interests. *Int J Adv Manuf Technol* 81:465–481
20. Busachi A, Erkoyuncu J, Colegrove P, Martina F, Ding J (2015) Designing a WAAM based manufacturing system for defence applications. *Procedia CIRP* 37:48–53. <https://doi.org/10.1016/j.procir.2015.08.085>
21. Rodrigues T, Duarte V, Miranda RM, Santos T, Oliveira JP (2019) Current status and perspectives on wire and arc additive manufacturing (WAAM). *Materials* 12:1121. <https://doi.org/10.3390/ma12071121>
22. Wang Y, Chen X, Konovalov SV (2017) Additive manufacturing based on welding arc: a low-cost method. *J Surf Invest-x-ray+* 11, 1317–1328
23. Xu XF, Ganguly S, Ding J, Seow CE, Williams S (2018) Enhancing mechanical properties of wire + arc additively manufactured Inconel 718 superalloy through in-process thermomechanical processing. *Materials & Design*, Volume 160, Pages 1042–1051, ISSN 0264–1275. <https://doi.org/10.1016/j.matdes.2018.10.038>
24. Zhang LN, Ojo OA (2020) Corrosion behavior of wire arc additive manufactured Inconel 718 superalloy. *J Alloys Compd* Volume 829, 154455 ISSN. <https://doi.org/10.1016/j.jallcom.2020.154455>
25. Asala G, Khan A, Andersson J, Ojo OA (2017) Microstructural analyses of ATI 718Plus produced by wire-ARC additive manufacturing process. *Metall and Mater Trans A* 48:1–18. <https://doi.org/10.1007/s11661-017-4162-2>
26. Yangfan W, Xizhang C, Chuanchu S (2019) Microstructure and mechanical properties of Inconel 625 fabricated by wire-arc additive manufacturing. *Surf Coat Technol* 374:116–123 ISSN 0257–8972. <https://doi.org/10.1016/j.surfcoat.2019.05.079>
27. Jan Hönnige, Cui Er Seow, Supriyo Ganguly, Xiangfang Xu, Sandra Cabeza, Harry Coules, Stewart Williams, Study of residual stress and microstructural evolution in as-deposited and inter-pass rolled wire plus arc additively manufactured Inconel 718 alloy after ageing treatment. *Materials Science and Engineering: A*, Volume 801 (2021) 140368. ISSN. <https://doi.org/10.1016/j.msea.2020.140368>
28. Jiang Qi, Zhang P, Zhishui Yu, Shi H, Li S, Wu Di, Yan H, Ye X, Chen J (2020) Microstructure and mechanical properties of thick-walled INCONEL 625 alloy manufactured by WAAM with different torch paths. *Adv Eng Mater*. <https://doi.org/10.1002/adem.202000728>
29. Bhujangrao T, Veiga F, Suarez A, Iriondo E, Mata F (2020) High-temperature mechanical properties of IN718 alloy: comparison of additive manufactured and wrought samples. *Crystals* 10:689. <https://doi.org/10.3390/cryst10080689>
30. Artaza T, Bhujangrao T, Suarez A, Veiga F, Lamikiz A (2020) Influence of heat input on the formation of laves phases and hot cracking in plasma arc welding (PAW) additive manufacturing of Inconel 718. *Metals* 10:771. <https://doi.org/10.3390/met10060771>
31. Kah P, Suoranta R, Martikainen J (2013) Advanced gas metal arc welding processes. *Int J Adv Manuf Technol* 67:655–674. <https://doi.org/10.1007/s00170-012-4513-5>
32. Tapiola J (2017) Cold metal transfer cladding of wear and corrosion resistant coatings in engine applications. <https://doi.org/10.13140/RG.2.2.15573.52963>
33. Selvi S, Vishvakshenan A, Rajasekar E (2018) Cold metal transfer (CMT) technology - an overview. In *Defence Technology* (Vol. 14, issue 1, pp. 28–44). Elsevier Ltd. <https://doi.org/10.1016/j.dt.2017.08.002>
34. <https://www.fronius.com/en/welding-technology/info-centre/magazine/2019/cmt-cycle-step>
35. Fung C (1978) “Strength of arc-spot weld in sheet steel construction”. AISI-Specifications for the Design of Cold-Formed Steel Structural Members. 148.
36. Whittenberger JD (1992) A review of: “superalloys II” edited by CT. Sims, N.S. Stoloff, and W.C. Hagel, A Wiley-Interscience Publication John Wiley & Sons, New York, NY 615 pages, hardcover, 1987. *Mater Manuf Proc* 7:3, 463–468. <https://doi.org/10.1080/10426919208947432>
37. <https://patents.google.com/patent/CZ306654B6/cs>
38. Jurić I, Garasić I, Bušić M, Kožuh Z (2018) Influence of shielding gas composition on structure and mechanical properties of wire and arc additive manufactured Inconel 625. *JOM*. <https://doi.org/10.1007/s11837-018-3151-2>
39. Baixo C, Dutra J (2011) Effect of shielding gas and transfer mode on the application of 625 alloy in carbon steel. *Weld Int* 25:903–909. <https://doi.org/10.1080/09507116.2010.527480>
40. Elango P, Sethuraman B (2015) Welding parameters for Inconel 625 overlay on carbon steel using GMAW. *Indian J Sci Technol* 8. <https://doi.org/10.17485/ijst/2015/v8i1/84309>
41. <https://elmemesser.lv/en/products/gas-in-cylinders/welding-and-cutting-gases/>
42. Mookara R, Seman S, Ren J, Amirthalingam M (2021) Influence of droplet transfer behaviour on the microstructure, mechanical properties and corrosion resistance of wire arc additively manufactured Inconel (IN) 625 components. *Weld World*. <https://doi.org/10.1007/s40194-020-1043-6>
43. Cheepu MM, Lee C, Cho S-M (2020) Microstructural characteristics of wire arc additive manufacturing with Inconel 625 by super-TIG welding. *Trans Indian Inst Met*. <https://doi.org/10.1007/s12666-020-01915-x>
44. Tanvir AN, Mohammad & Ahsan, Md. Rumman & Ji, Changwook & Hawkins, Wayne & Bates, Brian & Kim, Duck Bong. (2019) Heat treatment effects on Inconel 625 components fabricated by wire + arc additive manufacturing (WAAM)—part 1: microstructural characterization. *Int J Adv Manuf Technol*. <https://doi.org/10.1007/s00170-019-03828-6>
45. <https://www.specialmetals.com/documents/technical-bulletins/inconel/inconel-alloy-625.pdf>
46. Mašek P, Fornusek T, Zeman P, Bucko M, Smolik J, Heinrich P (2019) Machinability the aisi 316 stainless steel after processing by various methods of 3d printing. *MM Sci J* 3338–3346. https://doi.org/10.17973/MMSJ.2019_11_2019091
47. ASTM G99–05 Standard Test Method for Wear Testing with a Pin-on-Disk Apparatus
48. AlFaify A, Hughes J, Ridgway K (2019) Controlling the porosity of 316L stainless steel parts manufactured via the powder bed fusion process. *Rapid Prototyp J* 25(1):162–175. <https://doi.org/10.1108/RPJ-11-2017-0226>

Publisher's Note Springer Nature remains neutral with regard to jurisdictional claims in published maps and institutional affiliations.